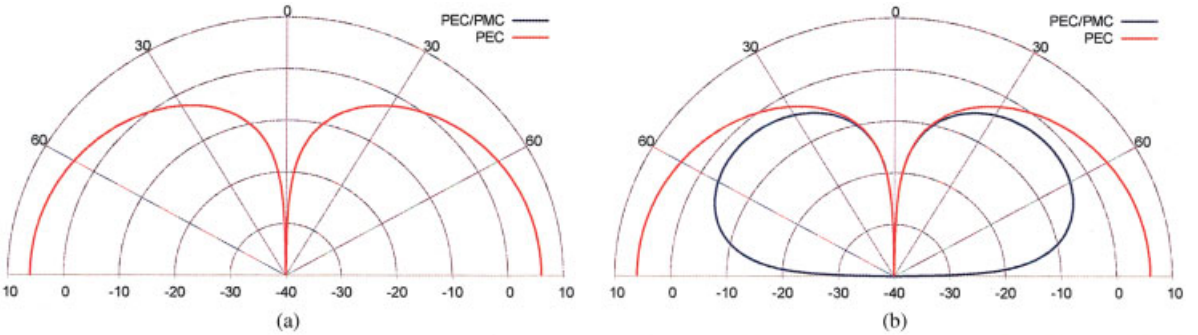

Figure 7 Comparison between normalized far-field radiation from a z-directed incremental electric dipole source at a height of $\lambda/8$ over an x-directed PEC/PMC strip surface (blue) and a PEC (red): (a) G_Θ at $\phi = 0°$; (b) G_Θ at $\phi = 90°$. [Color figure can be viewed in the online issue, which is available at www.interscience.wiley.com]

like a PMC surface for this direction of observation. It can also be noted that the fields are zero for $\theta = \pi/2$, except when $\varphi = 0$ and $\varphi = \pi$. Thus, the field will propagate along the surface in the direction of the strips, that is, in the direction for which the surface behaves like a hard surface. This corresponds to localized surface waves following the strips, as investigated for strip loaded scatterers in [10]. The far field from a vertical dipole (z-directed) over the PEC/PMC strip surface is shown in Figure 4, where once again the anisotropic property of the surface can be noted. It can also be noted that the behavior of E_θ and E_φ when θ is close to $\pi/2$ are almost interchanged compared to the case of the y-directed dipole.

Figures 5–7 show the normalized radiation patterns for incremental electric dipoles over PEC/PMC strip and PEC surfaces, respectively. In these plots, the dipole height over the plane has been chosen as $\lambda/8$. Once again, the fact that the PEC/PMC strip surface behaves as a PEC when the dipole is parallel to the strips is shown in Figure 5. When the dipole is oriented transverse to the strips of the PEC/PMC surface, the propagation along the surface is enhanced in H-plane while it is prevented for the PEC surface, as shown in Figure 6. When the dipole is normal to the surface, that is, z-directed, the radiation in direction transverse to the strips of the PEC/PMC strip surface is prevented, as shown in Figure 7. This fact can be used, for example, for reducing the coupling between monopoles, as compared to when they are mounted on a PEC plane (in which case the coupling is strong).

5. CONCLUSION

We have presented a dyadic reflection coefficient for the canonical PEC/PMC strip surface. The reflection coefficient can conveniently be used in GO, GTD, and spectral-domain computations or in cases when plane-wave reflection in this type of surface is of interest. We have also shown examples of computations of an electric dipole over the anisotropic surface using far-field approximation.

REFERENCES

1. W.E. McKinzie III and R.R. Fahr, A low-profile polarization diversity antenna built on an artificial magnetic conductor, IEEE AP-S Int Symp, San Antonio, TX, Jun., 2002, vol. 1, pp 762–765.
2. F. Yang and Y. Rahmat-Samii, Reflection-phase characterizations of the EBG ground plane for low-profile wire antenna applications, IEEE Trans Antennas Propagat 51 (2003), 2691–2703.
3. P.-S. Kildal, Artificially soft and hard surfaces in electromagnetics, IEEE Trans Antennas Propagat 38 (1990), 1537–1544.
4. P.-S. Kildal and A. Kishk, EM modeling of surfaces with STOP or GO characteristics: Artificial magnetic conductors and soft and hard surfaces, ACES Conf, Monterey, CA, 2003 (to appear in an ACES J special issue).
5. S. Chen, M. Ando, and N. Goto, Frequency characteristics and bandwidth enhancement of artificially soft and hard surfaces, IEE Proc Microwaves, Antennas Propagat 142 (1995), 289–294.
6. S. Chen, M. Ando, and N. Goto, Analytical expression for reflection coefficients of artificially soft and hard surfaces: Dielectric slab loaded with a periodic array of strips over a ground plane, IEE Proc Microwaves Antennas Propagat 142 (1995), 145–150.
7. I.V. Lindell, Image theory for the soft and hard surface, IEEE Trans Antennas Propagat 43 (1995), 117–119.
8. P.-S. Kildal, Foundations of antennas: A unified approach, textbook for Antenna design using Mathcad, Studentlitteratur, Sweden, 2000, www.studentlitteratur.se/antennas.
9. C.A. Balanis, Advanced engineering electromagnetics, Wiley, New York, 1989.
10. Z. Sipus, H. Merkel, and P.-S. Kildal, Green's functions for planar soft and hard surfaces derived by asymptotic boundary conditions, IEE Proc H 144 (1997), 321–328.

A METAMATERIAL-SCANNING NEAR-FIELD OPTICAL MICROSCOPE

H. Cory, Y. Hao, and C. G. Parini
Department of Electronic Engineering
Queen Mary University of London
Mile End Road
London E1 4NS, United Kingdom

Received 19 September 2005

ABSTRACT: *A metamaterial-scanning near-field optical microscope is proposed to study a subwavelength object consisting of a pair of long slits. The device comprises a metamaterial slab adjacent to the object and a subwavelength probe consisting of a single long slit which slides along the other side of the slab. A finite-difference time-domain (FDTD) simulation is performed, which provides the field-intensity contours outside the device. It is found that by using two slabs of different widths (with and without probe), in the cases considered, the resolution is better when the probe is present.* © 2006 Wiley Periodicals, Inc.
Microwave Opt Technol Lett 48: 587–590, 2006; Published online in Wiley InterScience (www.interscience.wiley.com). DOI 10.1002/mop.21415

Key words: *metamaterial slab; SNOM; FDTD; resolution*

INTRODUCTION

Generally, the behavior of a metamaterial slab, when it is used as a perfect lens in order to produce subwavelength images, is analyzed in two dimensions by assuming the existence of a virtual plane on the side where the object lies and the existence of another virtual plane on the side where the image lies. Pendry [1] has shown that a metamaterial slab can be used as a superlens which focuses evanescent modes and resolves objects only a few nanometers wide in the optical domain. Fang et al. [2] have reported an experimental subdiffraction-limited optical imaging with a silver superlens. But two stringent criteria have to be met when using this device [3]: the surface of the film must be extremely smooth and its thickness must be optimized. It would be interesting to find another way of retrieving the image with less stringent conditions: Alu et al. [4] have shown how metamaterial layers placed on the entrance and on the exit face of a subwavelength aperture in an opaque flat screen could be used to enhance the wave transmission through this aperture. In this paper, we propose an alternative implementation of the perfect lens by using the standard methods of scanning near-field optical microscopy (SNOM) [5] by inserting a metamaterial slab (instead of air or a dielectric slab) between the object and the probe.

THEORY

The diffracted spectrum of an object whose dimensions are much smaller than the wavelength consists of exponential (growing or decaying) and trigonometric (propagating) fields. Information on the geometry of this object is contained in the exponential components of the field. In the case of a dielectric slab, the probe (whose dimensions should be much smaller than the wavelength) is to be placed as close as possible to the object (the slab width should be much smaller than the wavelength), so that the exponential field should decay as little as possible as it recedes from the object. On the other hand, in the case of a metamaterial slab where the exponential field grows as it recedes from the object (tempered evidently by unavoidable losses), this is less relevant. According to [5], a small object lit by a propagating field generates a diffracted field that is partly exponential; conversely, by applying the reciprocity theorem, a small probe placed in an exponential field converts part of this field into a propagating field which could be detected in the far region. Let us suppose that the source is a plane wave of wavelength λ_0, approximately obtained through an array of ten linear sources situated close to an object consisting of two infinitely long slits in the x-direction, each one of very small width w ($w \ll \lambda_0$), as shown in Figure 1. Their separation s is very small ($s \ll \lambda_0$). The width of the metamaterial slab is denoted by d. The probe is an infinitely long slit in the x-direction, of very small width W ($W \ll \lambda_0$). It may be displaced up and down along the slab in the y-direction in order to achieve a point-by-point scanning of the object (Fig. 1). This is advantageous when we wish to scan only part of the object. Moreover, since a number of different probes are available, we can select the probe best suited to our needs. For instance, if the intensity obtained without any probe or with a given probe is too weak, we could use a vibrating metallic conical probe [6], which enhances the intensity. The metamaterials used in this paper are dispersive, their permittivity and permeability being described as follows:

$$\varepsilon(\omega) = \varepsilon_0\left(1 - \frac{\omega_{pe}^2}{\omega(\omega - j\nu_e)}\right),$$

H. Cory is on sabbatical leave from the Electrical Engineering Department, Technion, Technion City, Haifa 32000, Israel

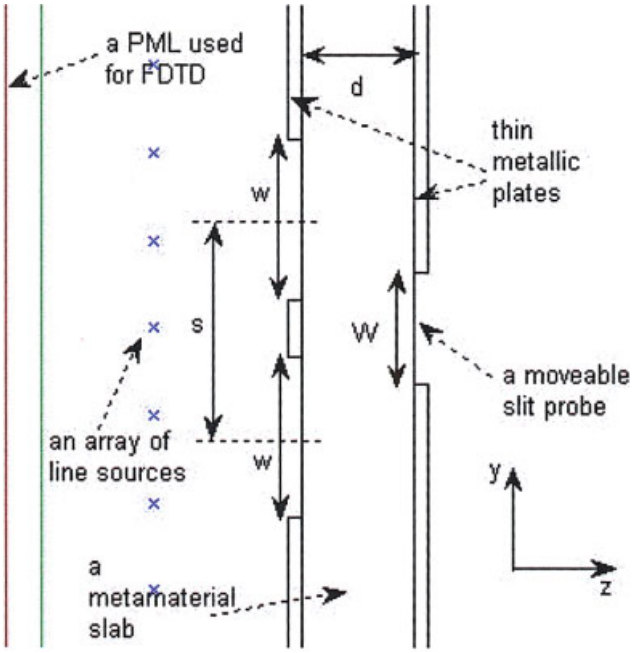

Figure 1 Geometry of the metamaterial SNOM. [Color figure can be viewed in the online issue, which is available at www.interscience.wiley.com]

$$\mu(\omega) = \mu_0\left(1 - \frac{\omega_{pm}^2}{\omega(\omega - j\nu_m)}\right),$$

where ω_{pe} and ω_{pm} are the electric and magnetic plasma frequencies, respectively. ν_e and ν_m are the electric and magnetic collision frequencies, respectively, and represent losses in the medium. In our study, both ν_e and ν_m are set equal to zero, assuming a lossless metamaterial.

Our theoretical analysis follows closely that given in [5] for a structure consisting of an object and a scatterer immersed in air. As pointed out in [5], this representation appears not to be strictly valid because it has been done under the Kirchhoff approximation. However, it was justified there using a completely self-consistent method, which has led to similar results.

The following theoretical analysis is intended to explain the physical processes involved in the SNOM performance. For the sake of simplicity, the object and the scatterer are both represented by an infinitely long slit and the metallic plates have zero thickness. The origin is taken at the center of the object. A monochromatic field $E_0(x, z)$ propagates along the z direction and impinges on the object situated at $z = 0$. Let us assume that, to a first approximation, the field just on the left-hand side of the object can be written as

$$E_1(x, z = 0) = E_0(x, z = 0^-) \cdot C\left(x, -\frac{w}{2}, +\frac{w}{2}\right)$$

for an infinitely long slit, where $C(x, -(w/2), +(w/2))$ is the rectangular function.

Let us denote by $E_1^*(k_x', z = 0)$ the Fourier transform of $E_1(x, z = 0)$. Then, we obtain

$$E_1^*(k_x', z = 0) = \int_{-\infty}^{+\infty} E_1(x, z = 0)e^{+jk_x'x}dx.$$

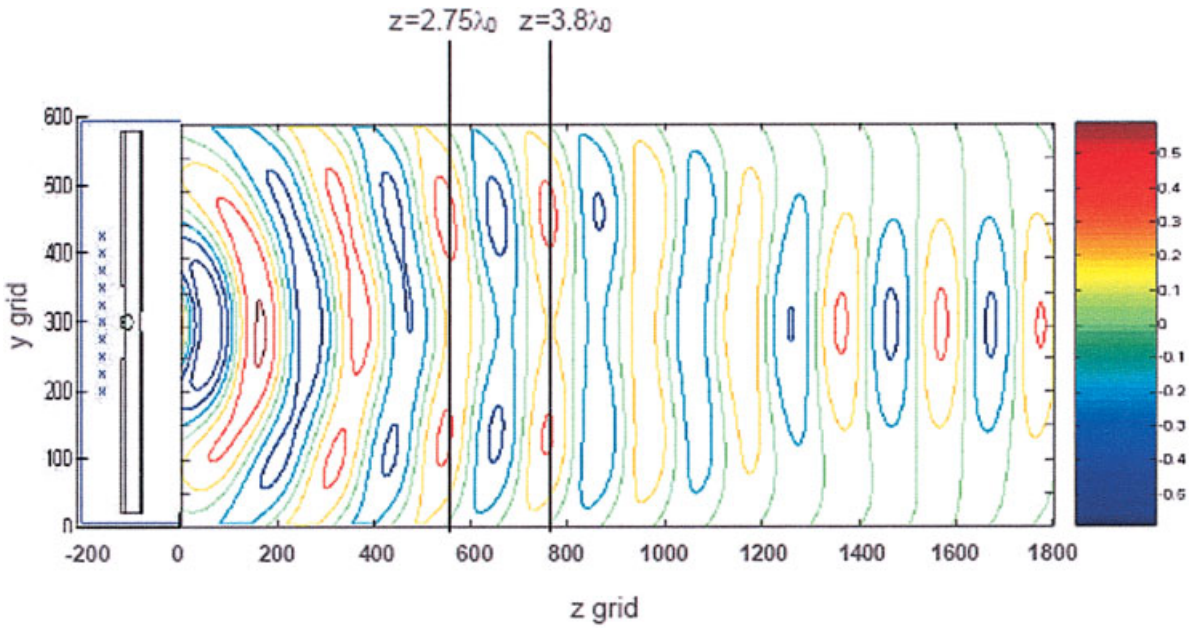

Figure 2 Electric-field intensity (v/m) contours in the y–z plane (400 cells corresponding to 1 μm). $y = 0$ is located 0.75 μm under the middle of the probe while $z = 0$ is located 0.25 μm to the right of the middle of the metamaterial slab. [Color figure can be viewed in the online issue, which is available at www.interscience.wiley.com]

The exponential field would have been lost if the slab was dielectric and its width $d \gg \lambda_0$. It would have contributed to the far field for a dielectric slab, after having been partially transformed into a propagating field by the scatterer, for a slab width $d \ll \lambda_0$. For a metamaterial slab, since the exponential field grows with distance, its width should not be necessarily much smaller than the wavelength. The electric field on the right-hand side of the object should therefore be given by

$$E_2(x, z = 0^+) = \int_{-\infty}^{+\infty} E_1^*(k'_x, z = 0) e^{-jk'_x x} dk'_x.$$

The total field at a distance d from the object on the left-hand side of the scatterer should be given by

$$E_2(x, z = d^-) = \int_{-\infty}^{+\infty} E_1^*(k'_x, z = 0) e^{-jk'_x x} e^{+j\sqrt{k^2 - k'^2_x}\, d} dk'_x,$$

where $k = \omega/v$ and v is the wave velocity in the metamaterial.

The + sign in the exponent is related to the metamaterial nature of the slab. The field on the aperture of the scatterer is given by

$$E_3(x, z = d) = \int_{-\infty}^{+\infty} E_1^*(k'_x, z = 0) e^{-jk'_x x} e^{+j\sqrt{k^2 - k'^2_x}\, d} dk'_x \cdot C\left(x, -\frac{W}{2}, +\frac{W}{2}\right)$$

for an infinitely long slit. Its Fourier transform is consequently given by

$$E_3^*(k_x, z = d) = \int_{-\infty}^{+\infty} E_3(x, z = d) e^{+jk_x x} dx.$$

The total field on the right-hand side of the scatterer is given by

$$E_4(x, z = d^+) = \int_{-\infty}^{+\infty} E_3^*(k_x, z = d) e^{-jk_x x} dk_x.$$

Finally, the far field at the detector (situated at $z = Z$), which contains only propagating components, is given by the following expression:

$$E_4(x, z = Z) = \int_{-\infty}^{+\infty} E_3^*(k_x, z = d) e^{-jk_x x} e^{-j\sqrt{k^2 - k_x^2}(Z-d)} dk_x,$$

which contains information on the geometry of the object.

SIMULATION

Let us assume that the center of the probe is located on the axis of symmetry of the device and let us choose $z = -\lambda_0/2$ in the middle of the metamaterial slab. We have used a dispersive FDTD simulation, but other numerical simulations are applicable [7]. We have taken $\lambda_0 = 0.5$ μm, $s = 0.0775$ μm, $w = 0.115$ μm, $d = 0.08$ μm, $\varepsilon/\varepsilon_0 = -1$, $\mu/\mu_0 = -1$, $W = 0.08$ μm, $\omega_{pe} = \omega_{pm} = \sqrt{2}\ \omega_0$. The metallic plates are 0.01-μm thick and assumed perfectly conducting. The FDTD cell size is $\lambda_0/200$ and the computational region is 2000 $\times$ 600 cells. An eight-layer uniaxial perfectly matched layer (UPML) is used as an absorbing boundary and only TM polarization is considered in our simulation. The field intensity contours in the y–z plane outside the device are shown in Figure 2. The field intensity is plotted in Figure 3 as a function of y at the fixed distances z, where it attains its highest values, that is, $z = 2.75\lambda_0$ and $z = 3.8\lambda_0$. The resolution (maximum intensity divided by minimum intensity) is good ($\sim$1.46) at $z = 3.8\lambda_0$. The simulation has been repeated without the probe (Fig. 4). It can be seen that in this case, the intensity is lower than in the previous case (about twice), the

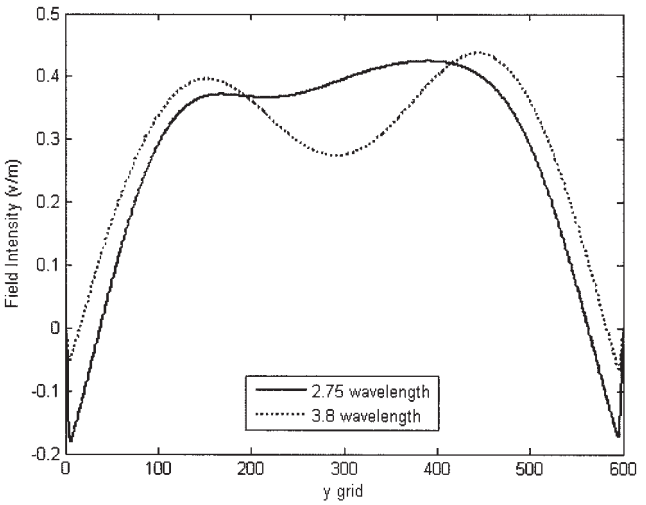

Figure 3 Resolution for an object consisting of two slits with probe present (400 cells corresponding to 1 μm)

resolution is lower ($\sim$1.26), and it occurs only at $z = 4\lambda_0$. There is no resolution at $z = 2.95\lambda_0$, showing that the focal region is narrower. Using a thin slab ($d = 0.04$ μm) instead of the previous thick one ($d = 0.08$ μm), it can be shown that when the probe is missing, the intensity is higher (about eightfold), the resolution is lower ($\sim$1.3 against $\sim$1.9), and the focal region is narrower. If we remove the metamaterial thick slab, leaving air between the object and the probe, we observe that the image is around 200 times weaker, showing the decisive influence of the metamaterial slab in obtaining high-intensity images.

CONCLUSION

A metamaterial scanning near-field optical microscope has been proposed. The object (consisting of a pair of long subwavelength slits) is separated from the probe (consisting of a long subwavelength slit) by a metamaterial slab. The probe slides along the slab. It has been found that by using two slabs of different widths (with and without probe) in the cases considered, the resolution is better when the probe is present. It is advantageous to use a probe when we wish to scan only part of an object. Moreover, since a number of different probes is available, we can select the probe best suited to our needs. A study is underway to optimize the various parameters and the components involved in the microscope in order to obtain the strongest intensity with the highest resolution.

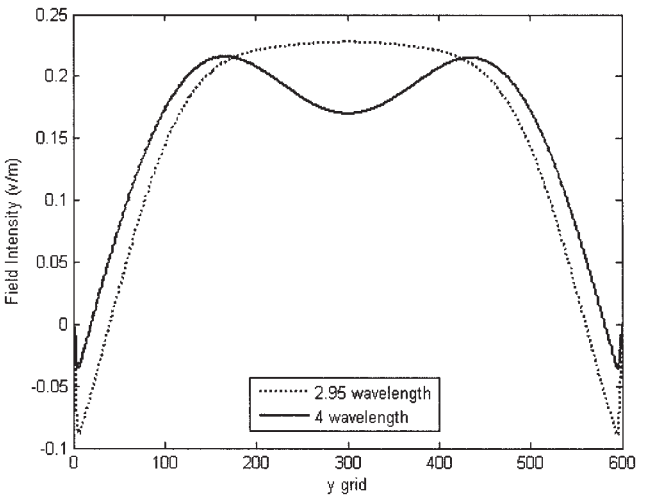

Figure 4 Resolution for an object consisting of two slits with probe missing (400 cells corresponding to 1 μm)

REFERENCES

1. J.B. Pendry, Negative refraction makes a perfect lens, Phys Rev Lett 85 (2000), 3966–3969.
2. N. Fang, H. Lee, C. Sun, and X. Zhang, Subdiffraction-limited optical imaging with a silver superlens, Sci 308 (2005), 534–537.
3. D.R. Smith, How to build a superlens, Sci 308 (2005), 502–503.
4. A. Alu, F. Bilotti, N. Engheta, and L. Vegni, How metamaterials may significantly affect the wave transmission through a subwavelength hole in a flat perfectly conducting screen, IEE Wkshp, London, Nov., 2003, pp 1–6.
5. J.M. Vigoureux, F. Depasse, and C. Girard, Superresolution of near-field optical microscopy defined from properties of confined electromagnetic waves, Appl Optics 31 (1992), 3036–3045.
6. H. Cory, A.C. Boccara, J.C. Rivoal, and A. Lahrech, Electric-field intensity variation in the vicinity of a perfectly conducting conical probe: Application to near-field microscopy, Microwave Opt Technol Lett 18 (1998), 120–124.
7. Y. Leviatan, Electromagnetic coupling between two half-space regions separated by two slot-perforated parallel conducting screens, IEEE Trans Microwave Theory Tech 36 (1988), 44–52.

WIDEBAND MINIATURE ANTENNA FOR IEEE 802.11 a AND 11b WLAN STANDARDS

M. Multari and R. Staraj
Laboratoire d'Electronique
Antennes et Télécommunications
Université de Nice-Sophia Antipolis/UMR-CNRS 6071
250 rue Albert Einstein, Bât. 4
Les Lucioles 1, 06560 Valbonne, France

Received 17 September 2005

ABSTRACT: *A compact, lightweight, low-cost, miniature dual-band printed antenna for 2.4-GHz (2.4–2.484 GHz) and 5.2-GHz (4.9–5.8 GHz) WLAN applications is presented. This antenna is dedicated to be integrated on a PCMCIA card. To optimize its behavior, this antenna combines several techniques, namely, the use of parasitic and shorted parasitic patches. The electromagnetic software simulator Agilent Momentum is used to optimize the structure and good agreement between the theoretical and measured results is obtained.* © 2006 Wiley Periodicals, Inc. Microwave Opt Technol Lett 48: 590–593, 2006; Published online in Wiley InterScience (www.interscience.wiley.com). DOI 10.1002/mop.21416

Key words: *miniature antenna; wideband antenna; wireless communications*

INTRODUCTION

Printed dipole antennas are very attractive for applications in WLAN systems. Many products are now designed to satisfy the IEEE 802.11a and 802.11b WLAN standards. Such antennas have the advantages of occupying a very small volume and having low-cost fabrication. They also have the merit to be made in a very simple way and to have omnidirectional radiation patterns. Several promising printed dual-band monopole antennas have also been demonstrated, which are suitable for applications in mobile units. For this purpose, this paper describes a dual-band-frequency F-shaped monopole printed antenna